Crystallography Reports, Vol. 49, No. 3, 2004, pp. 357–369. From Kristallografiya, Vol. 49, No. 3, 2004, pp. 422–434.

DIFFRACTION AND SCATTERING OF IONIZING RADIATIONS

Indicators of the Magnetic State in the Charge Distributions of MnO, CoO, and NiO. II: Para- and Antiferromagnetism of CoO[1]

J.-P. Vidal*, G. Vidal-Valat*, and K. Kurki-Suonio**

** Laboratoire d'Analyse Multipolaire des Répartitions de Charges Expérimentales, Université Montpellier 2, 34095 Montpellier Cedex 05, France*

e-mail: jpgvidal@univ-montp2.fr

*** Department of Physics, P.O. Box 64, FIN–00014 University of Helsinki, Finland*

Received July 2, 2002

Abstract—X-ray diffraction intensities from CoO were measured above and below the Néel temperature. The data were submitted to a non-parametric multipole analysis aiming at formulation of experimentally valid statements on the nature of the charge distribution. Strong "bonding maxima" are seen between the Co ⟨110⟩O nearest neighbors. In the paramagnetic state they are formed by the Co-ion alone, in the antiferromagnetic state they involve a strong CoO coupling. The outer electrons of oxygen give rise to slight maxima in the ⟨110⟩ directions, making the atom into an O^{2-} ion. In the paramagnetic state, their coupling with the bonding feature forms an octahedral electron cage around each oxygen atom. Broad density maxima between the atoms in ⟨111⟩ directions are present in both states. They connect the "bonding maxima" in the ⟨110⟩ directions, more strongly in the antiferromagnetic state, building up an interatomic three-dimensional network. Such electron network structures seem to be characteristic of metal oxides more generally. © *2004 MAIK "Nauka/Interperiodica".*

1. INTRODUCTION

This is the second part of an investigation aiming at finding characteristics of the different magnetic states of the first-row transition metal monoxides MnO, CoO, and NiO with the help of a multipole interpretation of their charge densities based on accurate X-ray diffraction data. This paper reports the experiments performed, interpretational procedures used in the case of cobalt oxide, and the conclusions reached on its para- and antiferromagnetic states.

Our principle of interpretation is completely different from the conventional parametric multipole analysis. It does not aim at any sophisticated models that would fit the data, but at the formulation of experimentally valid statements on the nature of the charge distribution that would be as independent as possible of any models. As has been shown repeatedly in earlier papers on direct multipole analysis, a simple reference model is sufficient to achieve this. Results that are expressed in terms of the radial multipole scattering factors and accumulation-of-charge densities of the single atoms do not depend on the reference model, as long as it is "asymptotically valid." It is argued that, in the Fourier representation of the charge density, only such features can be significant as arise from low order multipole components of the ionic distributions. Moreover, comparison of the Fourier representation with the multipole densities of the ions allows one to conclude how the electrons of the different ions contribute to the features found to be significant, as in [1].

The electronic states of transition-metal monoxides have been studied intensively over several decades using many different experimental methods and an abundance of theoretical models with an increasing degree of sophistication. In this respect, there is little to be added to the introductory review of Vidal-Valat, Vidal, K. Kurki-Suonio, and R. Kurki-Suonio in [2].

Bredow and Gerson [3] have made quantum chemical calculations on bulk properties of MgO, NiO, and CoO with various periodic models. They have found that, for NiO and CoO, a combination of the Hartree-Fock exchange functional with the Lee-Young-Parr density functional correlation is the best method in terms of relative stability and geometry and the electronic structure of the valence band.

Recently, Neubeck [4] has made an extensive study of antiferromagnetic MnO, CoO, and NiO by X-ray magnetic scattering. Using nonresonant magnetic scattering, they found nonzero orbital moments in CoO and NiO, which is contrary to what was earlier thought. In comparing their experimental resonance scattering amplitudes with modeled amplitudes based on spin-orbit perturbated crystal field states, they found a good agreement for MnO and NiO, but not for CoO.

Neubeck [4] also presents an excellent review of the development of our understanding of the magnetic structure of these compounds. From this, it is clear that CoO differs from MnO and NiO in some essential

[1] This article was submitted by the authors in English.

respects. For instance, the magnetic moment of CoO is not in the (111) plane, as it is in the case of NiO and MnO, as concluded by Laar [5] and Hermann-Ronzaud, Burlet, and Rossat-Mignot [6] from their neutron studies.

Obviously, the observed properties of CoO have been the most difficult of these three monoxides to interpret, and its electronic structure is not yet understood. Our accurate X-ray diffraction study of its charge distribution may make a new contribution. Preliminary results of this investigation have been available on videotape (Vidal *et al.* [7]) for some time.

2. EXPERIMENTAL PROCEDURES

A single crystal of CoO of full stoichiometry was kindly provided by the Laboratoire de Chimie des Solides, Université d'Orsay (France). It was synthesized by float-zone refining techniques from high-purity powder 5N. By this method, a high degree of mosaicity is produced, minimizing the effect of extinction on the diffracted intensities so that conventional extinction corrections are satisfactory as stated by Vidal, Vidal-Valat, and Zeyen [8]. The full stoichiometry of the crystal was checked and confirmed by optical and crystallographic methods, as reported by Revcolevschi [9].

The crystal was cleaved several times parallel to the (001) crystal faces. It was hard and, when sufficiently thin, optically fully transparent with a light garnet-red color. Cleaving below a certain size reduced the crystal, however, to small pieces. The sample chosen for the X-ray diffraction measurements was a parallelepiped of size $0.134 \times 0.191 \times 0.217$ mm^3. Sometimes, the surface of cleavage was somewhat streaked. The faces of the sample used were, however, seen to be perfectly smooth. The freshly cleaved sample was coated with plastic to avoid oxidization. This protection was seen to be perfectly transparent to the X-ray beam.

The first measurements were made on the grown sample in its freshly cleaved state. It was, however, impossible to obtain acceptable data. A slight random motion of the Bragg peaks around their positions during data registration was observed, this causing random variations in the collected intensities as well. At the same time, background scattering was very high, and reflections beyond $\sin\theta/\lambda = 0.85$ Å^{-1} did not emerge from it. In particular, the *hhh* reflections were suppressed the more strongly the higher *h* was.

These phenomena, which were observed to be similar in both of the magnetic phases, are probably caused by the presence of a high number of vacancies formed in the growth of the crystals and their migration, which is enhanced by the strong magnetostriction in the magnetic phase transition. However, within a year, all these disturbing effects vanished. The *hhh* reflections recovered their intensities. No more motion of the Bragg peaks was observed, and the background scattering attained a normal level, in accordance with the requirements of accurate registration of intensities. Thus, a complete experiment was conducted. The reflections with the most regular profiles were chosen for further analysis.

An accurate X-ray diffraction study of CoO was carried through both above and below the Néel temperature—at 298 K for the paramagnetic phase and 85 K for the antiferromagnetic phase. The temperature was controlled to within ±1 K. Neither a magnetic field nor mechanical stress was applied to the sample in the X-ray diffraction measurements.

Relative integrated intensities of all reflections up to about 1 Å^{-1} in $\sin\theta/\lambda$ in three octants were collected three times in both temperatures on an automated four-circle Enraf-Nonius CAD–4 diffractometer with MoK_α radiation. The data thus obtained consisted of 26 independent reflections. Equivalent reflections differing in integrated intensity by >4% from the average were discarded. The excluded reflections were seen to be randomly distributed. The observed intensity of a reflection was taken to be the mean of the remaining symmetry-related reflections.

The integration was done in the θ-2θ scan mode with programmed scan and aperture at the scanning speed of 2 arcmin s^{-1}. The dead-time correction was automatically taken into account by the analyzer.

The multiple-scattering effect was eliminated by setting the crystallographic and diffractometer axes differently. As a check, all forbidden reflections were measured in a whole octant. No effect was detected.

Background, Lorentz and polarization corrections were made on the intensities, as described by Vidal, Vidal-Valat, Galtier, and Kurki-Suonio [10], as well as the absorption corrections of Busing and Levy [11], using the linear absorption factors 21.696 mm^{-1} and 21.850 mm^{-1} for CoO at 298 and 85 K, respectively.

TDS contaminations were evaluated with the program of Merisalo and Kurittu [12] using the elastic constants of Subhadra and Sirdeshmuk [13]. The effects were small—less than 3% in intensity—owing to the hardness of these compounds.

The data registration was made in terms of the observed triclinic unit cell. The systematic extinctions of the Bragg intensities show, however, that the structure in both phases is very close to the cubic NaCl structure of the symmetry group $Fm\bar{3}m$. Least-squares refinement based on X-ray diffraction patterns yielded the lattice constants 4.260(4) and 4.250(4) Å for the cubic cell at 298 and 85 K, respectively.

The atomic distances corresponding to the ideal cubic structure differ from the real distances by, at most, 0.1%. The analysis was based on the cubic cell.

3. TREATMENT OF DATA

The data were submitted to "direct multipole analysis," as described in the first part of our study on MnO. All that was said about the analysis in that context on the reference model and on the representation of results holds in this case, even in detail, except for data referring specifically to the Co atom and to the numerical values used or obtained, and will not be repeated here.

For the Co^{2+} ion of the reference model, the relativistic Hartree-Fock values of [14] were used with the anomalous scattering factors $f' = 0.299$ and $f'' = 0.973$ by Cromer and Liberman [15] for MoK_α.

Also for CoO, the isotropic mosaic-spread extinction gave lower R factors, 0.010 and 0.013, than particle-size extinctions, which were 0.011 and 0.014 at 298 and 85 K, respectively, and yielded the values $0.035(5) \times 10^4$ rad^{-1} and $0.036(7) \times 10^4$ rad^{-1} for the mosaic spread parameter g and $B_{Co} = 0.366$ (0.035) Å^2, $B_O = 0.516$ (0.052) Å^2 and $B_{Co} = 0.365$ (0.016) Å^2, $B_O = 0.497$ (0.071) Å^2 for the isotropic Debye-Waller factors in 298 and 85 K, respectively. No more significant improvement was obtained by any of the more sophisticated models.

In the successive iterative local Fourier-refinement of the scale and the Debye-Waller factors (cf. Vidal-Valat, Vidal, K. Kurki-Suonio, and R. Kurki-Suonio [16]), the scale factors remained unchanged, while $B_{Co} = 0.348$ Å^2, $B_O = 0.516$ Å^2 and $B_{Co} = 0.348$ Å^2, $B_O = 0.506$ Å^2 were obtained as the final refined values of the Debye-Waller factors of the reference model for 298 and 85 K, respectively.

The results are represented by figures and tables as in the case of MnO.

Table 1 gives the final experimental structure factors, F_0, on an absolute scale, corrected for isotropic mosaic-spread extinction and for anomalous dispersion, together with the extinction factors y and the standard errors of the mean δF_0.

Figure 1 shows the radial accumulation-of-charge densities $s_{i0}(r_i)$ and the radial electron counts $Z_{i0}(R_i)$ around the ionic sites.

Table 2 is related to Fig. 1 and, as spherical characteristics of the ionic charge distributions, gives:

(1) The radii r_0 of best separation at which the radial accumulation-of-charge densities $s_0(r)$ reach their minima, as a measure of the size or the effective "range" of the ionic charge distribution.

(2) The corresponding minimum radial density $s_{0min} = s_0(r_0)$, as a measure of the inseparability of the ion from its surroundings.

(3) The electron count $Z_0 = Z_0(r_0)$ within the radius of best separation as a measure of the charge concentrated in the main bulk of the ionic charge density peak.

Table 1a. Structural factors for CoO at 298 K

h k l	2sinθ/λ, Å^{-1}	F_0	F_c	δF_0	y
0 0 0	0.0000		140.000		
1 1 1	0.4066	60.7835	60.2010	0.3300	0.846
2 0 0	0.4695	97.8882	98.6173	0.5800	0.681
2 2 0	0.6639	79.5798	78.2897	0.5000	0.849
3 1 1	0.7786	45.6229	45.9879	0.2100	0.944
2 2 2	0.8132	63.9447	65.4940	0.3100	0.909
4 0 0	0.9390	57.5381	56.5804	0.3100	0.947
3 3 1	1.0232	35.8417	35.8621	0.2000	0.977
4 2 0	1.0498	50.5362	50.0001	0.2400	0.952
4 2 2	1.1500	45.0762	44.9557	0.2000	0.968
3 3 3	1.2197	25.9159	29.3344	0.1600	0.988
5 1 1	1.2197	28.7003	29.3344	0.1600	0.988
4 4 0	1.3279	37.0973	37.7667	0.2000	0.979
5 3 1	1.3887	25.3801	24.9804	0.1800	0.991
4 4 2	1.4084	34.5427	35.1216	0.2000	0.987
6 0 0	1.4084	34.6821	35.1216	0.1900	0.982
6 2 0	1.5393	32.9947	32.9011	0.2000	0.988
5 3 3	1.5571	22.1988	21.9456	0.1500	0.994
6 2 2	1.6263	30.7432	31.0044	0.1600	0.990
4 4 4	1.6263	26.3238	29.3579	0.1400	0.991
5 5 1	1.6764	20.5625	19.7211	0.1100	0.994
7 1 1	1.6764	19.2766	19.7211	0.1200	0.996
6 4 0	1.6927	28.0562	27.9076	0.1300	0.989
6 4 2	1.7566	27.1865	26.6129	0.1200	0.991
5 5 3	1.8031	18.0288	18.0025	0.1000	0.996
7 3 1	1.8031	17.9282	18.0025	0.1000	0.996
8 0 0	1.8779	24.4096	24.3760	0.1200	0.994

Table 1b. Structural factors for CoO at 85 K

h k l	2sinθ/λ, Å^{-1}	F_0	F_c	δF_0	y
0 0 0	0.0000		140.000		
1 1 1	0.4075	60.2018	60.1711	0.3500	0.840
2 0 0	0.4706	97.1731	98.5045	0.6000	0.672
2 2 0	0.6655	80.0369	78.1600	0.5300	0.843
3 1 1	0.7804	45.8626	45.8925	0.2200	0.942
2 2 2	0.8151	63.2570	65.3664	0.3400	0.906
4 0 0	0.9412	56.8815	56.4612	0.3200	0.945
3 3 1	1.0256	35.1756	35.7553	0.2000	0.976
4 2 0	1.0523	50.7228	49.8912	0.2500	0.950
4 2 2	1.1527	44.5647	44.8567	0.2200	0.966
3 3 3	1.2226	24.5571	29.2315	0.1600	0.988
5 1 1	1.2226	28.5452	29.2315	0.1600	0.988
4 4 0	1.3110	37.2309	37.6875	0.2100	0.978
5 3 1	1.3920	25.4383	24.8850	0.2000	0.990
4 4 2	1.4118	34.2523	35.0508	0.2000	0.986
6 0 0	1.4118	34.4353	35.0508	0.2000	0.981
6 2 0	1.4881	33.3573	32.8376	0.2000	0.988
5 3 3	1.5429	21.7674	21.8572	0.1500	0.994
6 2 2	1.5608	31.6652	30.9471	0.1600	0.984
4 4 4	1.6302	24.7864	29.3059	0.1500	0.990
5 5 1	1.6803	20.3818	19.6381	0.1200	0.994
7 1 1	1.6803	19.5570	19.6381	0.1200	0.995
6 4 0	1.6967	27.7776	27.8599	0.1300	0.988
6 4 2	1.7608	27.0272	26.5688	0.1300	0.991
5 5 3	1.8073	18.0272	17.9231	0.1000	0.996
7 3 1	1.8073	17.9013	17.9231	0.1100	0.996
8 0 0	1.8823	24.3714	24.3373	0.1300	0.994

Table 2. Spherical characteristics of the ionic electron distributions

Co^{2+}	r_0, Å	s_{0min}, *e*/Å	Z_0, *e*	r_{2+}, Å
Experimental				
298 K	1.05	4.419	25.0	1.05
85 K	1.05	2.186	24.88	1.10
Reference model				
298 K	1.10	3.975	25.18	1.05
85 K	1.10	4.012	25.19	1.055
O^{2-}	r_0, Å	s_{0min}, *e*/Å	Z_0, *e*	r_{2-}, Å
Experimental				
298 K	0.92/1.40	4.57/5.36	7.25/9.92	1.42
85 K	0.85/1.37	5.00/5.10	6.93/9.87	1.40
Reference model				
298 K	1.15	4.570	8.69	1.40
85 K	1.15	4.600	8.69	1.39

Note: r_0 is the radius of best separation at which the radial accumulation-of-charge density $s_0(r)$ reaches its minimum, the minimum radial density $s_{0min} = s_0(r_0)$, the electron count $Z_0 = Z_0(r_0)$ within the radius of best separation, and the r_{2+} and r_{2-} are the radii where the electron counts reach the values 25*e* and 10*e* corresponding to the doubly ionized states

(4) The radii r_{2+} and r_{2-}, where the electron counts reach the values 25*e* and 10*e* corresponding to the doubly ionized states.

Figure 2 presents the radial multipole scattering factors $f_{in}(b; R_i)$ as deviations from the reference model. The partitioning radii R_{Co} = 1.15 Å and R_O = 1.30 Å were deduced on the basis of Fig. 1 and were taken to be slightly larger than the radii r_0 of best separation, as in Kurki-Suonio [17]. For oxygen, the same radius has been used in all of our oxide studies. With their error bars, the figures indicate the significance of the components with respect to the errors of mean of the structure factors. All components up to the 10th order were calculated. The components of order 4, 6, and 8 are of about equal significance, while the 10th-order component is insignificant and is not shown. These are the primary results of the multipole analysis from which the significance of the different features of the real space distributions are concluded.

Figure 3 shows, for sake of visualization and easier interpretation, the same components in real space in terms of the multipole accumulation-of-charge densities $s_{in}(r_i)$ around the ionic sites as deviations from the reference model. The areas under the curves $Z_{in}(R_i)$ give the electron counts under the positive lobes of $K_n(\theta, \varphi)$ within the radii R_i. These multipole electron counts serve as non-spherical integral characteristics of the ionic charge distributions as indicated by the numbers given in the figures.

To facilitate understanding of the curves in Figs. 2 and 3, the angular behavior of the relevant harmonics is shown at each of the curves as a reduced map-on-sphere.

In Fig. 4, the results are visualized in terms of difference-density maps representing the multipole expansions at the ionic sites, as composed of the components shown in Figs. 2 and 3. For each ion, maps of the three main lattice planes—(100), (110), and (111)—through the ionic site are shown. For comparison, the conventional Fourier difference-density maps on the same planes are shown. This comparison is important.

Finally, Fig. 5 shows views of the three-dimensional nature of the ionic multipole expansions to support the discussion of results.

Colored versions of Fig. 5 are available at the Internet address www.cines.fr/EWUS.

4. DISCUSSION

Comparison of the radial densities s_0 of the reference model at the two temperatures, shown by dotted lines in Fig. 1 and by the corresponding parameters in Table 2, shows that the effect of the temperature factors on the nature of the ionic charge distributions is negligible. The differences between the experimental curves and parameters at the two temperatures are, thus, of electronic origin and can be attributed to differences of the magnetic states. These are evident in the deviations of the experimental curves from the reference curves in Fig. 1 and in the numerical values of Table 2. They are shown in a larger scale by the Δs_0 curves of Fig. 3.

The radial density $s_0(r)$ of the oxygen has a peculiar feature. Based on earlier observations on oxide peaks (cf. Vidal-Valat, Vidal, and Kurki-Suonio [18] and Vidal-Valat, Vidal, K. Kurki-Suonio, and R. Kurki-Suonio [19]), one would expect a separating minimum to occur in the overlap region, as in the case of MnO. However, there is, similarly in both magnetic states, an intermediate maximum that is stronger than one would expect in the case of simple covalent bonding. In addition, the outer part of the main density peak is strongly compressed as compared with the reference model, while it is slightly expanded in MnO. In Table 2, values corresponding to both minima are given. The maximum makes the separation of oxygen from its surroundings ambiguous. If the maximum is included in the oxygen, the peak electron count comes to about 10*e*, corresponding to O^{2-}, the radii r^{2-} being just slightly larger, while in MnO, as well as in the earlier observations, the oxide peak comes to 9*e*.

In both states of CoO, the separating minimum of the cation is deeper and sharper than in the reference model, while, in the paramagnetic MnO, some flattening was stated. Together with a slight increase of density at smaller *r*, this gives the impression of the cation being compressed. This leads to rather well-defined radii of best separation. The electron counts of the cat-

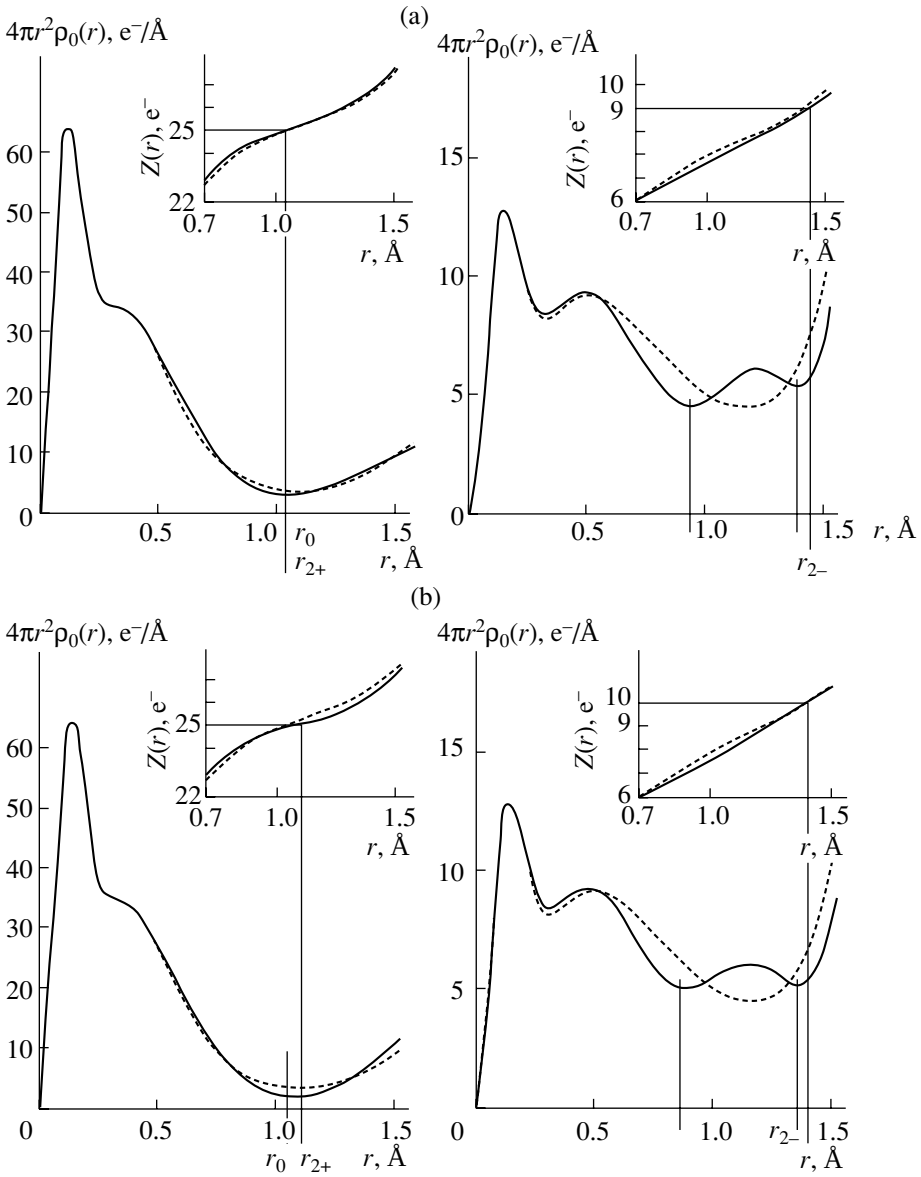

Fig. 1. Radial accumulation-of-charge densities $s_0(r)$ and electron counts $Z_0(r)$ around the ionic sites of Co^{2+} and O^{2-}, experimental (solid lines), reference model (dashed lines). (a) The paramagnetic state (298 K); (b) the antiferromagnetic state (85 K). The radii r_0 of "best separation" or minimum s_0 and the radii r_{2+} and r_{2-}, where the electron counts correspond to double ionization of the ions, are indicated for the experimental curves.

ion peaks correspond very closely to the doubly ionized state Co^{2+} with 25*e* in both states. In the paramagnetic state of CoO, the density $s_0(r_0)$ at the minimum equals that of MnO. Like MnO, it decreases in the phase transformation to the antiferromagnetic state, even getting significantly lower. The values are, however, remarkably higher than one would expect for an ion (cf. Vidal-Valat, Vidal, and Kurki-Suonio [18] and Vidal, Vidal-Valat, Galtier, and Kurki-Suonio [10]).

To understand the origin of these spherical average features, it is necessary to find out how they arise from the three-dimensional ionic distributions built up from low-order multipole components. The radial multipole scattering factors $f_{in}(b; R_i)$ of Fig. 2 and their error bars form the basis for making a judgment about the empirical significance of the components. The radial accumulation-of-charge densities Δs_n of Fig. 3 show, as described in the first part of our study, how the significant multipoles contribute to the three-dimensional ionic electron densities [2].

The density maps of Fig. 4 form the final tool of the analysis. To facilitate the perception of their connections in three dimensions, the representative lines of a number of main crystallographic directions are drawn in one set of maps. In the local map representations, only those features are significant that are significant in

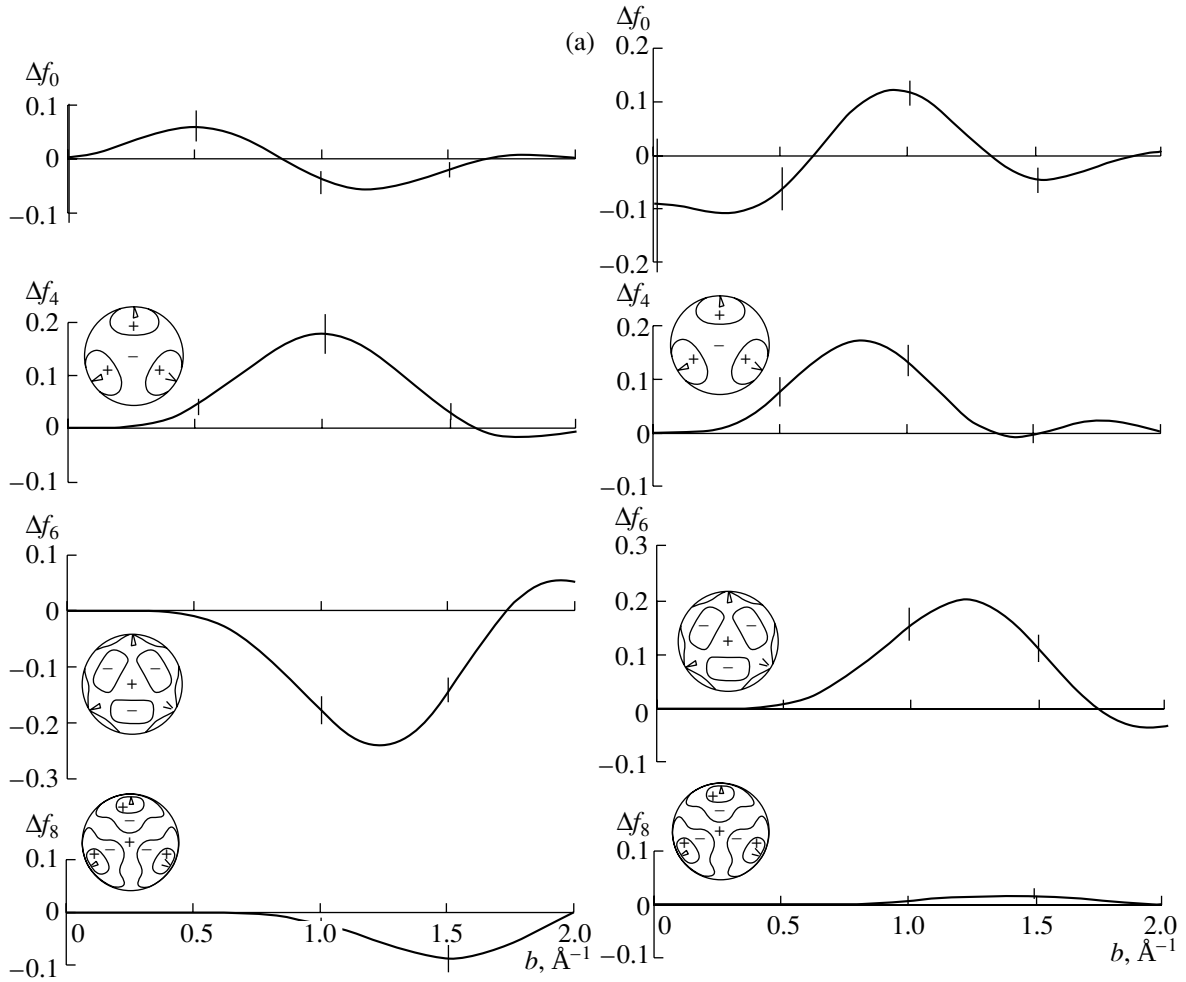

Fig. 2. Radial multipole scattering factors of the ions Co^{2+} and O^{2-} within the partitioning radii R_{Co} = 1.15 Å and R_O = 1.30 Å. The results refer to cubic harmonics normalized to the maximum value $K_n(\theta, \varphi) = 1$, and the curves represent deviations Δf_n from the reference model. (a) The paramagnetic state (298 K); (b) the antiferromagnetic state (85 K).

the angular-integral representation of Fig. 3. Thus, no attention need be paid to the difference densities at the ionic centers in any of the maps. Similarly, local features of the Fourier maps, which do not appear in the multipole maps of Fig. 4, do not arise from the integral systematics of the low-order multipoles and must be regarded as insignificant. Comparison with the multipole maps makes it possible to note how the features seen in the Fourier maps originate from the different atoms (Kurki-Suonio [1]).

The results are discussed in terms of three significant features, which are labeled A, B, and C for their identification in the different maps and in the three-dimensional representation of Fig 5.

A: Feature A looks much like covalent CoO bonding. It consists of density maxima between the nearest neighbors, Co⟨100⟩O, within the radius r_{2+} of Co. However, according to the multipole maps, it has a different electronic origin in the two magnetic states. In the paramagnetic CoO, it is built up almost solely by cation electrons, while in the antiferromagnetic CoO, where it is also clearly stronger, both ions contribute.

B: Feature B has maxima in the ⟨110⟩ directions from the oxygen site. It can be identified in all the maps through the oxygen site. It is a pure oxygen feature, lies within the oxygen radius r_{2-}, and is obviously responsible for the intermediate maxima in the radial density $s_0(r)$ of oxygen in Fig. 1.

C: Feature C consists of broad maxima between the O⟨111⟩Co neighbors. Although it lies outside any reasonable ionic partitioning spheres of the atoms, it definitely belongs to the low-order multipole behavior of both ions at the same time. It is, thus, understood to be significant, contrary to the maxima observed at these sites in MnO, and is interpreted to originate from a Co⟨111⟩O coupling. It dominates the view in Fig. 5, where it resembles triangular "pillows" fixed at the vertices of a cube in which the ion lies in the middle.

All three features A, B, and C, as such, are clearly stronger in the antiferromagnetic than in the paramag-

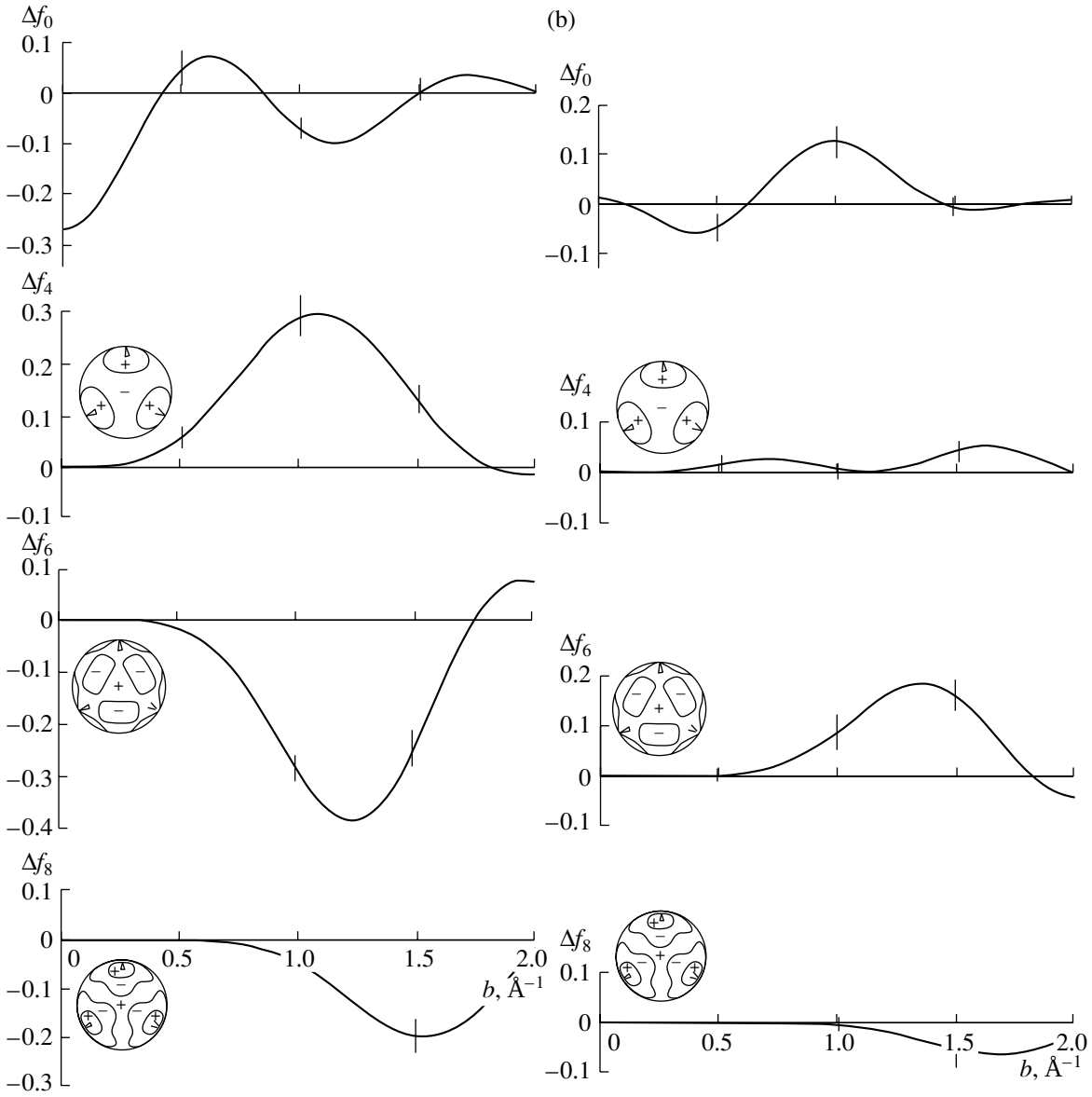

Fig. 2. (Contd.)

netic phase. While the multipole maps indicate how these features originate from the electrons of the different ions, the Fourier maps show how these features are coupled together, building up a complicated three-dimensional electronic network in the space between the atoms. Three types of possible couplings can be noted. The resulting networks seem to be different in the two magnetic states due to different mutual roles of these couplings.

ABA, oxygen cages: A and B build up an octahedral arrangement around each oxygen ion. The maxima of A lie at the vertices and the maxima of B in the middle of the edges of the octahedron, as seen in Fig. 5.

In the paramagnetic state, the oxygen feature B and the bonding feature A are closely coupled. Continuous ABA bridges are formed along the edges of the octahedron. Each oxygen atom becomes, thus, closed into its own electronic cage, which has the shape of an octahedron, and this is clearly visible in Fig. 5.

In the antiferromagnetic state, this coupling has largely vanished. There are no more of the continuous ABA bridges that built up the octahedral cage. On the other hand, the internal coupling of oxygen electrons that is responsible for feature B is stronger. This is shown from its tightness—it is significantly closer to the oxygen center, as can be seen also from the position of the intermediate maximum of the radial density $s_0(r)$ in Fig. 1—and from the slightly more unified ring formation surrounding oxygen in the (111) plane.

ACA: From the (110) Fourier maps, we note that the ⟨111⟩-intercation feature C connects the maxima of the

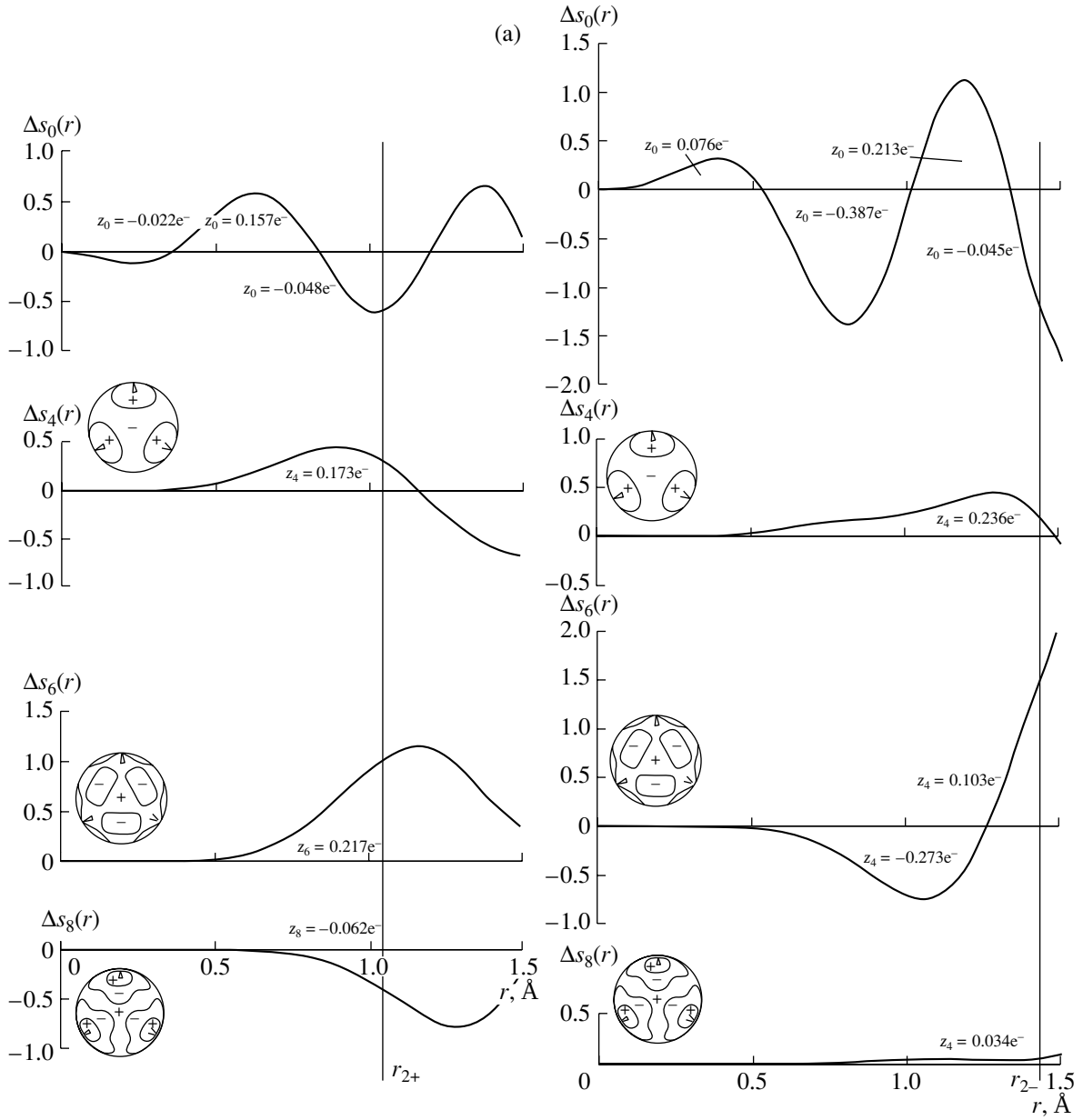

Fig. 3. Multipole accumulation-of-charge densities $s_n(r)$ around the ionic sites of Co^{2+} and O^{2-}. The curves represent deviations Δs_n from the reference model. (a) The paramagnetic state (298 K); (b) the antiferromagnetic state (85 K).

bonding feature A, and, in the paramagnetic state, the vertices of the neighboring octahedral cages, into more or less unified linear chains …CACA… on both sides of the ⟨110⟩ arrays of oxygen ions. These chains, running in the intermediate space between the ions in all symmetry-equivalent directions ⟨110⟩, build up a complicated three-dimensional electronic network. This network structure is clearly stronger and more unified, and, hence, the interactions responsible for this ACA coupling must be stronger in the antiferromagnetic state. Noting that A was found to be an internal phenomenon of Co in the paramagnetic state and a CoO coupling phenomenon in the antiferromagnetic state and that C was interpreted as originating from an O⟨111⟩Co interaction, we realize that the nature of this coupling is different in the two magnetic states and quite sophisticated in both.

BCB: The (111) Fourier maps through the oxygen site also give some indication of a possible BCB coupling of feature B of different oxygen atoms into (111) planar net structures with the aid of feature C. This indication is slightly stronger in the antiferromagnetic state. However, the empirical significance of this coupling remains unclear, since it is not visible in the multipole maps.

Formation of electron net structures in the interatomic space seems to be a general phenomenon in

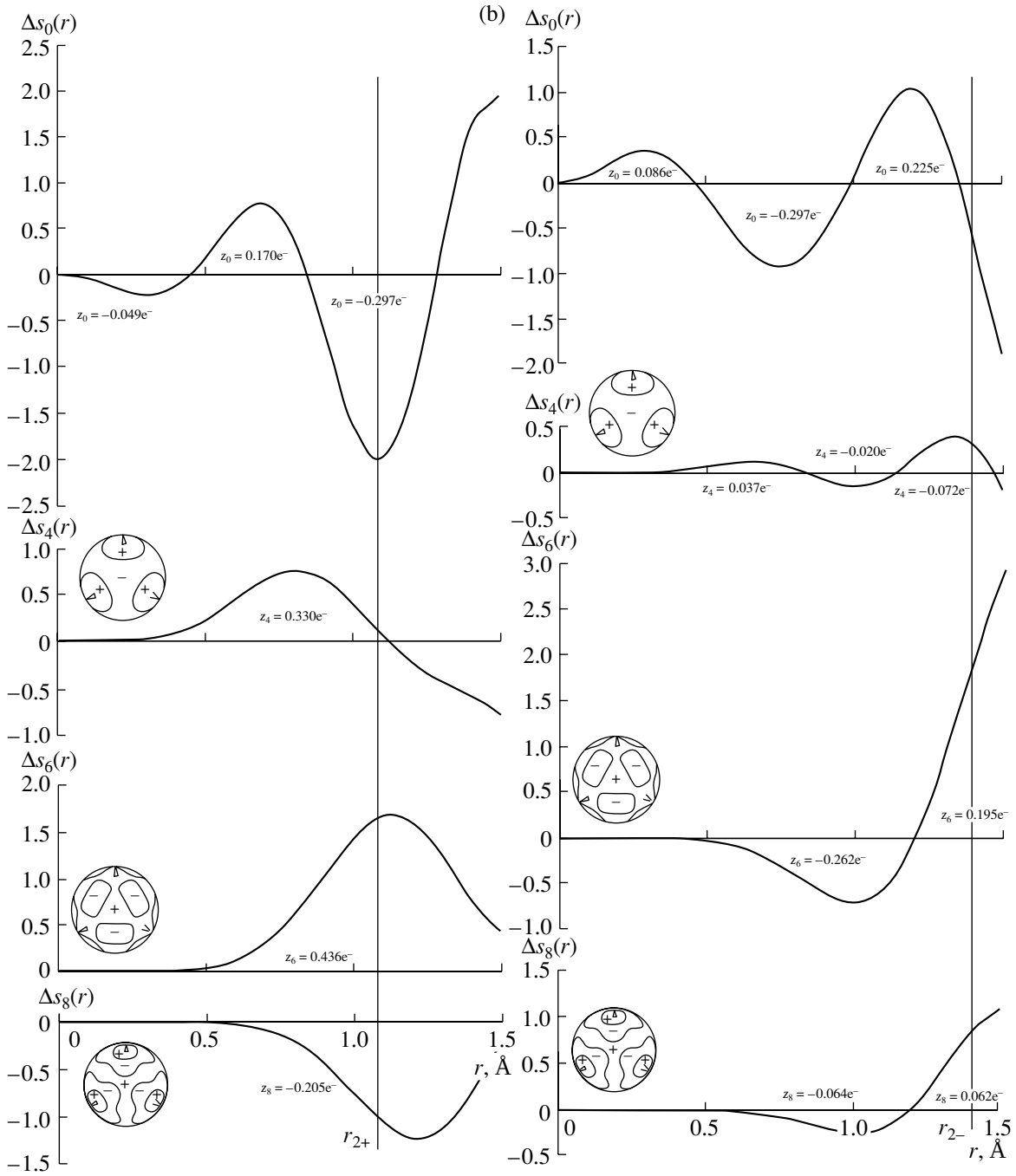

Fig. 3. (Contd.)

metal oxides (cf. the first part of our study). In MnO, this appeared as a three-dimensional network with the oxygen atoms in its cage-like pockets. In CoO, a comparable network is found that, however, is much more complicated. In the paramagnetic CoO, each oxygen has an octahedral cage of its own with its "walls" inside the radius r_{2-}, and the three-dimensional net is formed by connecting the vertices of these octahedra, while, in MnO, the oxygen cages were just pockets of the net outside the radius r_{2-} of double ionization. The couplings responsible for the cage formation and for the net buildup are obviously different in the two magnetic states. In the antiferromagnetic state, the net buildup, and with it the cage formation, were less obvious in MnO, while in CoO the cages have vanished but the net build-up is essentially stronger.

The problem of estimating the significance of such features in real space as revealed by the present method of analysis, in comparison with the accuracies obtained for the model parameters in the traditional fitting meth-

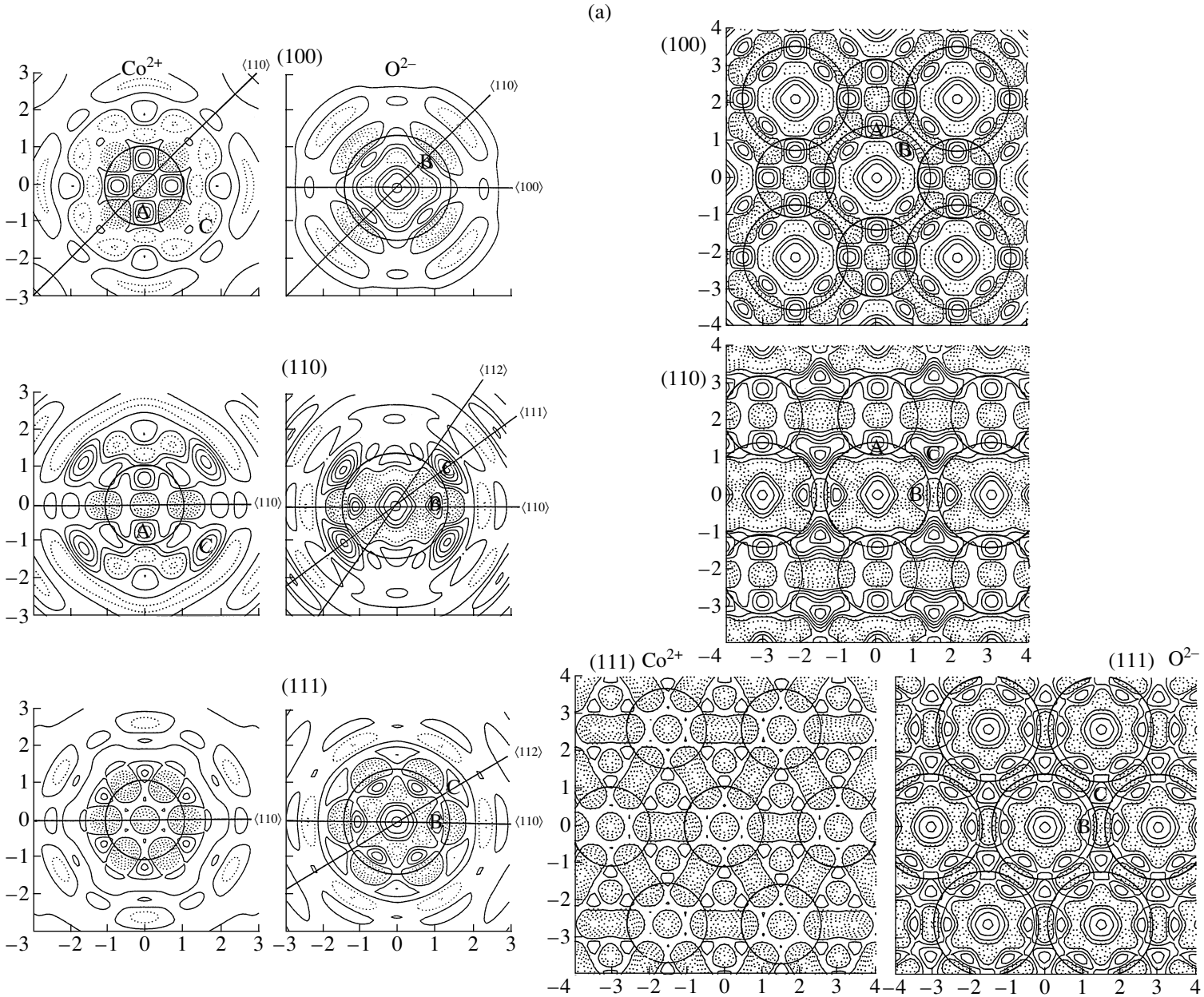

Fig. 4. Difference density maps of the multipole expansions up to $n = 8$ together with the corresponding Fourier difference-density maps on the lattice planes (100), (110), and (111) through the ionic sites. The circles indicate the radii of doubly ionized ions. (a) The paramagnetic state (298 K); (b) the antiferromagnetic state (85 K). Solid line positive, dashed line negative, and dotted line zero.

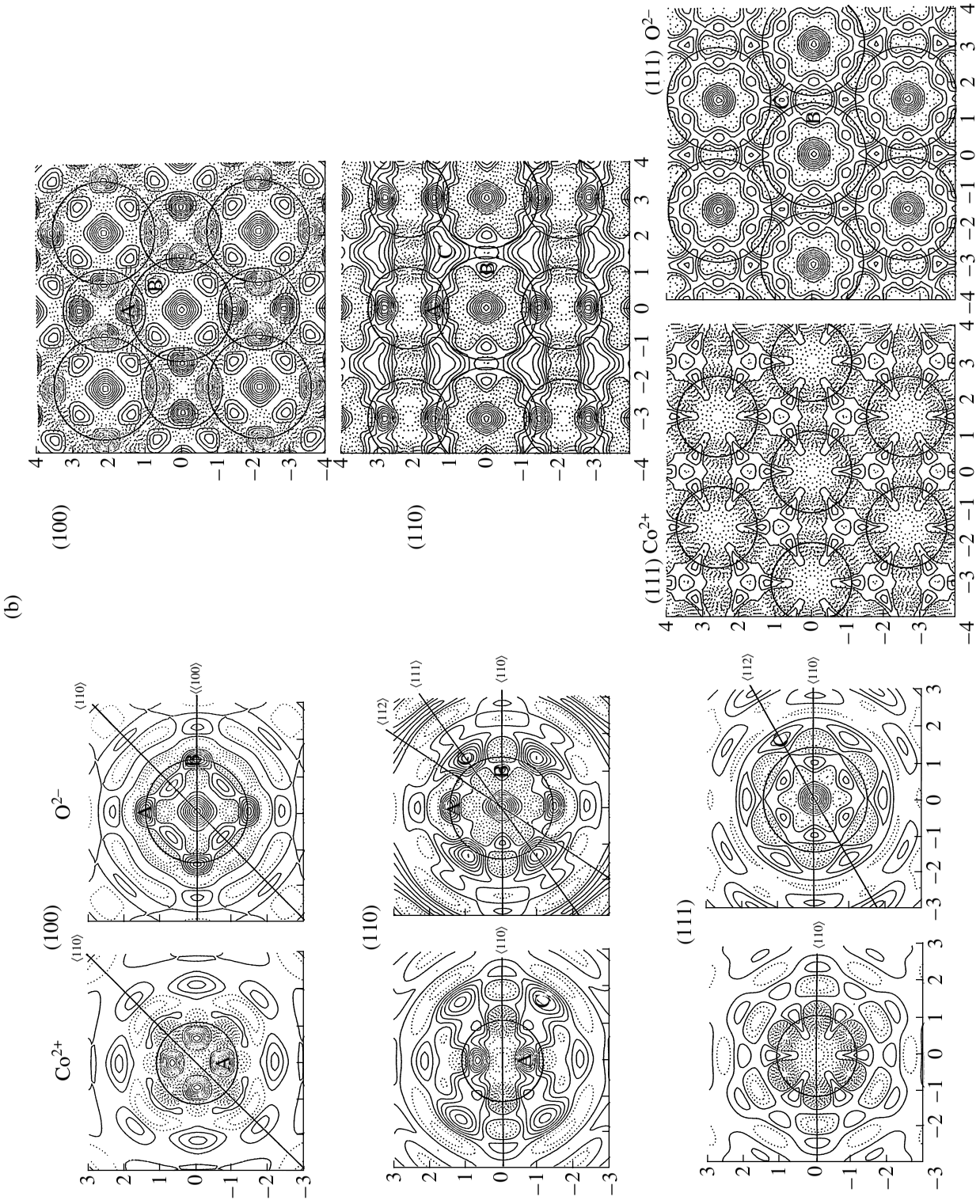

Fig. 4. (Contd.)

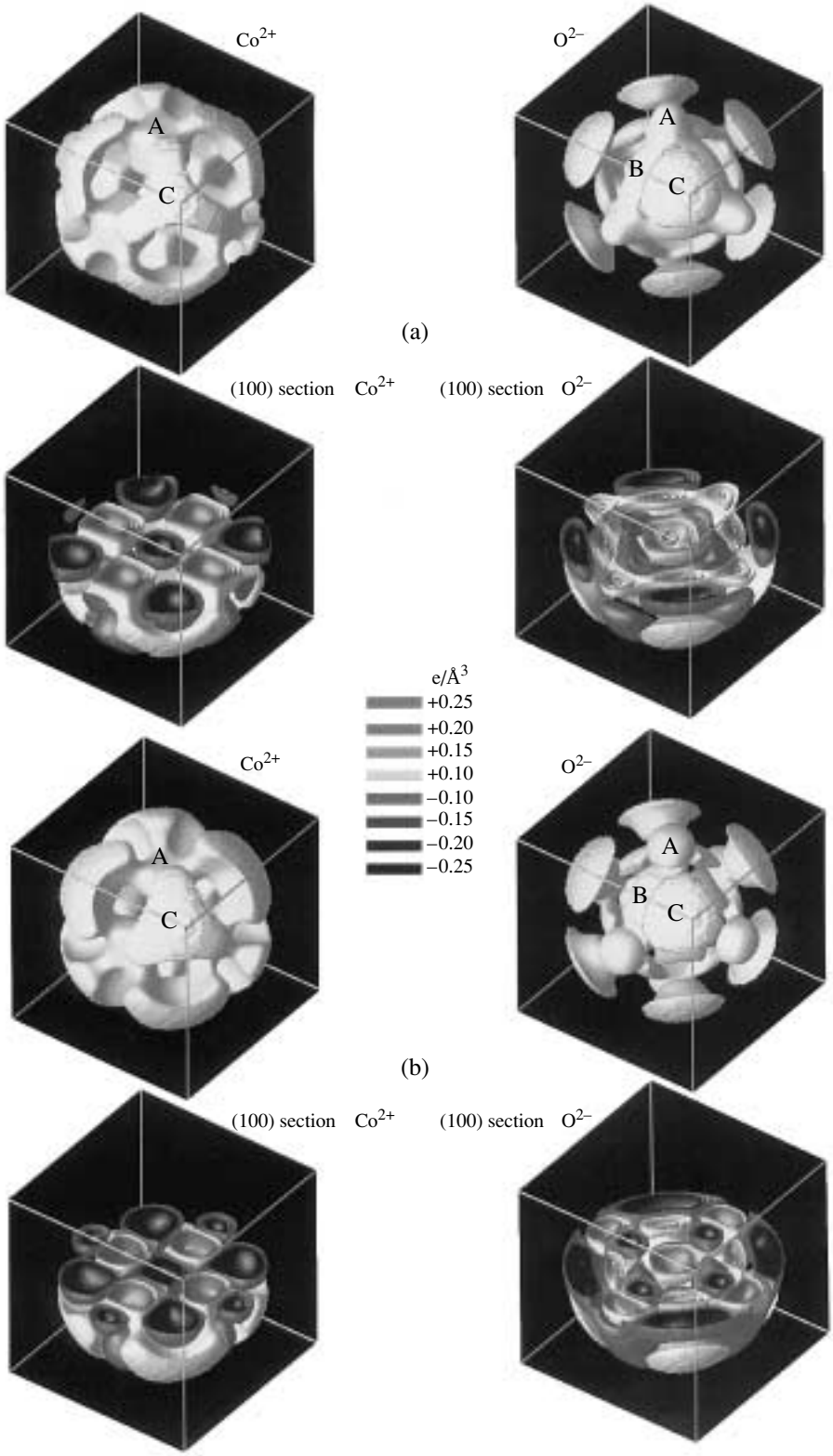

Fig. 5. Three-dimensional view of the equivalue surfaces of the ionic multipole expansions. (a) The paramagnetic state (298 K) within the radii R_{Co} = 1.3 Å, R_O = 1.8 Å; (b) the antiferromagnetic state (85 K) within the radii R_{Co} = 1.5 Å, R_O = 1.8 Å. For colors, see www.cines.fr/EWUS.

ods, has been discussed by Kurki-Suonio [1]. While the significance or insignificance is merely due to the accuracy of the measured data, it is expressed only by the error bars in $\Delta f_n(b)$, reflecting the large-scale integral nature of the information, and cannot be transformed into local accuracy statements. Local features can be regarded as significant to the relative extent expressed by the error bars insofar as they are parts of the integral multipole behavior.

ACKNOWLEDGMENTS

We thank the Centre Informatique National de l'Enseignement Supérieur (Montpellier, France) for financial support and technical assistance.

REFERENCES

1. K. Kurki-Suonio, in *Proceedings of Symposium Franco-Finlandais. Structure de la Matiére, Repartitions Electroniques dans les Cristaux, Paris, 1993*, Ed. by J.-P. Vidal (Montpellier, 1994), p. F1; in *Honour of the 75th Anniversary of Academician Boris Vainshtein*, Ed. by V. Simonov (Nauka, Moscow, 1996), p. 46.
2. J.-P. Vidal, G. Vidal-Valat, K. Kurki-Suonio, and R. Kurki-Suonio, Kristallografiya **47** (3), 391 (2002) [Crystallogr. Rep. **47**, 347 (2002)].
3. T. Bredow and A. R. Gerson, Phys. Rev. B **61** (8), 5196 (2000).
4. W. Neubeck, PhD Thesis (Univ. de Grenoble I, 2000).
5. B. V. Laar, Phys. Rev. **138**, 584 (1965).
6. D. Hermann-Ronzaud, P. Burlet, and J. Rossat-Mignot, J. Phys. C: Solid State Phys. **11**, 2123 (1978).
7. J.-P. Vidal, K. Kurki-Suonio, G. Vidal-Valat, and R. Kurki-Suonio, in video-film *The Wonderful World of the Crystal*, Ed. by J.-P. Vidal (Service du Film de Recherche Scientifique, Ministére de l'Education Nationale, Vanves, France, 1994).
8. J.-P. Vidal, G. Vidal-Valat, and C. M. E. Zeyen, Nucl. Instrum. Methods Phys. Res. A **228**, 569 (1985).
9. A. Revcolevschi, Rev. Int. Hautes Temp. Refract. **7**, 73 (1970).
10. J.-P. Vidal, G. Yidal-Valat, M. Galtier, and K. Kurki-Suonio, Acta Crystallogr., Sect. A: Cryst. Phys., Diffr., Theor. Gen. Crystallogr. **37**, 826 (1981).
11. W. R. Busing and H. A. Levy, Acta Crystallogr. **10**, 180 (1978).
12. M. Merisalo and J. Kurittu, J. Appl. Crystallogr. **11**, 179 (1978).
13. K. G. Subhadra and D. Sirdeshmukh, Indian J. Pure Appl. Phys. **16**, 693 (1978).
14. *International Tables for X-ray Crystallography* (Kluwer Academic, Dordrecht, 1999), Vol. C.
15. D. T. Cromer and D. Liberman, J. Chem. Phys. **53**, 1891 (1970).
16. G. Vidal-Valat, J.-P. Vidal, K. Kurki-Suonio, and R. Kurki-Suonio, Acta Crystallogr., Sect. A: Found. Crystallogr. **48**, 46 (1992).
17. K. Kurki-Suonio, Acta Crystallogr., Sect. A: Cryst. Phys., Diffr., Theor. Gen. Crystallogr. **24**, 379 (1968).
18. G. Vidal-Valat, J.-P. Vidal, and K. Kurki-Suonio, Acta Crystallogr., Sect. A: Cryst. Phys., Diffr., Theor. Gen. Crystallogr. **34**, 594 (1978).
19. G. Vidal-Valat, J.-P. Vidal, K. Kurki-Suonio, and R. Kurki-Suonio, Acta Crystallogr., Sect. A: Found. Crystallogr. **43**, 540 (1987).